Received September 9, 2020, accepted September 23, 2020, date of publication September 28, 2020,
date of current version October 21, 2020.

Digital Object Identifier 10.1109/ACCESS.2020.3027067

Matching Linear Chirplet Strategy-Based Synchroextracting Transform and Its Application to Rotating Machinery Fault Diagnosis

ZEHUI HUA, JUANJUAN SHI, AND ZHONGKUI ZHU
School of Rail Transportation, Soochow University, Suzhou 215131, China

Corresponding author: Juanjuan Shi (jshi091@suda.edu.cn)

This work was supported by the National Natural Science Foundation of China under Grant 51605319 and Grant 51875376.

ABSTRACT Various time-frequency analysis methods have been employed for the vibration signal processing of rotating machinery under time-varying speeds. However, most methods suffer from time-frequency blurriness, particularly for signals experiencing fast changes of instantaneous frequencies. Synchroextracting Transform is a powerful post-processing tool of time-frequency analysis; its results, nevertheless, greatly depend on the original time-frequency representation. This paper proposes a matching linear chirplet based synchroextracting transform to address the problem. Chirp-rate matching strategy is firstly developed to alleviate smearing problems of time-frequency representations, where the chirp-rates adaptively match true ones of signals with the guidance of kurtosis. The matching strategy is then integrated with synchroextracting transform to further sharpen the time-frequency representation. With enhanced energy concentration level and sharpened instantaneous frequency ridges, the readability of time-frequency representation can be improved, which is also echoed by more accurate extracted instantaneous frequency ridges. Rotating machinery fault diagnosis can then be realized based on the extracted time-frequency ridges.

INDEX TERMS Fault diagnosis, instantaneous frequency estimation, synchroextracting transform, time-frequency analysis, time-varying speed.

I. INTRODUCTION

Rotating machines are extensively used in industry. Bearings and gears are their key components; therefore, their maintenance is crucial for the normal operation of rotating machinery [1]. To minimize unscheduled downtime and economic losses, fault detection and diagnosis in key components of machinery are of great importance. It is clear from previous studies that vibration signal analysis is an effective method for the fault diagnosis of rotating machinery and has been widely employed in industry [2]–[6]. However, when rotating machines are operated under time-varying speed conditions, traditional techniques—which have been devised for constant-speed conditions—may be ineffective [7].

In light of this, order analysis is an effective method for rotating machinery fault diagnosis at varying speeds. Wang *et al.* conducted order analysis for bearing-fault diagnosis using the resampling strategy [8]. To successfully apply order analysis for use in fault diagnosis, the instantaneous frequency (IF) must be pre-extracted to map the non-stationary signal in the time domain to a stationary signal in the fault-phase angle domain. The crucial step of the method used in [8] is to obtain IF. However, the direct measurement of IF is often impossible when a tachometer cannot be used, which limits the applicability of this technique [9].

Time-frequency analysis (TFA) has also been widely applied for processing rotational machinery vibration signals under variable-speed conditions, as this type of analysis can simultaneously reveal detailed information in both the time and frequency domain [10]. The IF information can then be extracted from the time–frequency representation (TFR). However, vibration signals of rotating machinery are often affected by background noise, and fault-related IF ridges are suppressed by noise and interference, particularly for weak faults. To facilitate the extraction of IF ridges that contain rich information regarding the condition of the machinery [11]–[13], various TFA methods have been developed to enhance the readability of TFR.

The associate editor coordinating the review of this manuscript and approving it for publication was Gerard-Andre Capolino.

This work is licensed under a Creative Commons Attribution 4.0 License. For more information, see https://creativecommons.org/licenses/by/4.0/

To solve the potential time-frequency (TF) diffusion, methods such as iterative generalized demodulation and the iterative generalized synchrosqueezing transform have been proposed and have proven to be effective [14], [15]. Using these methods, more accurate IF estimations from the improved TFR can be extracted, which leads to more reliable fault diagnosis. Further, demodulation is used for enhancing the TF energy concentration levels. An iterative operation is designed to effectively tackle vibration signals of rotating machinery, which usually contain multiple frequency components. For instance, a vibration signal usually contains the shaft IF-related component, fault characteristic frequency component, their harmonics, and background noise. To further mitigate this problem, Ma *et al.* proposed generalized demodulation in combination with adaptive chirp-mode decomposition to decompose the signal [16]. The aforementioned synchrosqueezing transform (SST) is used to redistribute the TFR alongside the frequency components of interest, which acts as a post-processing technique to reassign the TF distributions [17]–[20]. Relying on a high-order estimation of IF, Tu *et al.* proposed the demodulated high-order synchrosqueezing method to overcome the TF diffusion caused by the rapidly varying IF [21]. Similar to the idea of demodulation, the linear chirplet transform (LCT) can also be adopted to enhance the TFR [22]. However, when dealing with non-stationary signals with frequencies experiencing rapid changes, an individual LCT usually fails to improve the TFR readability, particularly for cases where the IF of the analyzed signal exhibits non-linearly changing patterns. By advancing the LCT, generalized linear chirplet transforms (GLCTs) are proposed by iteratively employing a string of chirp rates to better match the frequency changes [23]. Nevertheless, when the TFR is enhanced using the appropriate chirp rate, the side effects—such as extra cross-terms caused by inappropriate chirp rates—cannot be neglected in the TFR.

In terms of post-processing of the TFR, the synchroextracting transform (SET)—developed based on the SST mentioned above—has also proven to be a powerful tool [24]. The main advantage of the SET is that it can retain the TF distributions around the true IFs with several frequency bins at a given instant in time, which greatly sharpens the TF ridges on the TFR. However, the SET suffers from heavy TF blurriness caused by background noise, which constrains the applicability of this method in the industry [25], [26]. In addition to the original SET, several variants have also been developed. One of these is the synchroextracting chirplet transform, proposed to acquire more accurate IF estimation [27]. The shortcoming of this method is that it is based on GLCT; hence, the cross-term interferences and additional TF blurriness inherently induced by GLCT cannot be avoided. To alleviate the cross-term interferences and simultaneously take advantage of the capability of sharpening the IF ridges of the SET, a potential solution is to obtain an enhanced TFR without cross-term interference and blurriness to facilitate the implementation of the SET, which is the motivation of the proposed method.

To overcome the cross-term interference caused by GLCT, especially when the frequency components are located close to one another and the signal is contaminated by heavy noise, the chirp-rate matching strategy is proposed, where proper chirp rates can be adaptively selected through the guidance of the kurtosis index and the iteration operations required for processing multi-component signals can be avoided. In order to further sharpen the IF ridges, the matching strategy is combined with the SET to form the proposed method, referred to as matching linear chirplet synchroextracting transform (MLCSET). Then, TFRs with improved readability can be obtained for rotating machinery abnormality detection and diagnosis.

The remainder of this paper is organized as follows. In section II, a detailed presentation of the proposed method is given. Next, the proposed TFA method is tested through simulations in section III. In section IV, a simulated bearing fault signal is first used to illustrate the effectiveness of the proposed method in obtaining more accurate time-varying features. Then, two experimental signals are used to further validate the effectiveness of the proposed method in dealing with non-stationary vibration signals in section IV. The conclusions of the study are drawn in section V.

II. PROPOSED MLCSET

A. MATCHING LINEAR CHIRPLET STRATEGY TO ENHANCE THE TFR

Based on the TFR enhancement strategy used in LCT, the matching linear chirplet transform (MLCT) is proposed. For a signal $s(t)$, the enhanced TFR can be formulated as

$$S_\alpha(u,\omega) = \int_{-\infty}^{+\infty} s(t)\, g(t-u) \times e^{-j\omega\left((t-u)+0.5\tan\alpha(u)(t-u)^2\right)} \mathrm{d}t \quad (1)$$

where $s(t)$ is the analyzed signal, $g(t)$ is the window function, and $\alpha(u)$ represents the inclination angle of an IF trajectory of a windowed signal centered at the time instant $t = u$. This can be done because the IF of a signal segment in a short window can be considered to be a straight line. Therefore, the angle $\alpha(u)$ can be considered as an indicator to measure the slope of IF of the windowed signal at time instant $t = u$, as well as the modified angle of the linear transforming kernel. In comparison to the original linear transforming kernel used in short-time Fourier transforms (STFTs), it can be seen that (1) degrades to the STFT when $\alpha(u) = 0$. Although the STFT can reveal changes in frequency with time, it is more suitable for processing signals with slowly time-varying features. In other words, the linear transforming kernel with an angle $\alpha(u) = 0$ is more suitable for processing signals with slowly varying frequencies. The angle $\alpha(u)$ in (1) has a profound influence on the TFR of the signal analyzed. Generally, the closer the angle to the true angles of the windowed signal, the more concentrated the energy level is. The highest energy concentration level is achieved when the selected $\alpha(u)$ is identical to the true inclination angle of the truncated signal.

The detailed proof is given as follows:

$$
\begin{aligned}
&|S_\alpha(u,\omega)| \\
&= \left| \int_{-\infty}^{+\infty} x(t)\, g(t-u)\, e^{-j\omega(t-u)} e^{-0.5j\omega\tan\alpha(u)(t-u)^2} \mathrm{d}t \right| \\
&= \left| \int_{-\infty}^{+\infty} e^{j\left(\omega(t-u)+0.5\omega'(u)(t-u)^2\right)} g(t-u) \right. \\
&\quad \left. \times e^{-j\omega(t-u)} e^{-0.5j\omega\tan\alpha(u)(t-u)^2} \mathrm{d}t \right| \\
&= \left| \int_{-\infty}^{+\infty} e^{0.5j\left(\omega'(u)-\omega\tan\alpha(u)\right)(t-u)^2} g(t-u)\, \mathrm{d}t \right| \\
&\le \int_{-\infty}^{+\infty} \left| e^{0.5j\left(\omega'(u)-\omega\tan\alpha(u)\right)(t-u)^2} \right| \cdot |g(t-u)|\, \mathrm{d}t \\
&= \int_{-\infty}^{+\infty} |g(t-u)|\, \mathrm{d}t \\
&= \left| \int_{-\infty}^{+\infty} g(t-u)\, \mathrm{d}t \right| \qquad (2)
\end{aligned}
$$

where ω' denotes the first derivative of the IF and the physical interpretation of ω' is the slope of the IF. The window $g(t)$ used here is a real symmetric function. To ensure independence from any prior knowledge regarding IFs, a series of discrete angles α are used, helping to find the matching frequency of windowed signals. The physical interpretation of this equation is that when the selected chirp rate of the signal (defined here as $\omega \times \tan\alpha$) reflects the actual value (ω'), the TFR will achieve the most energy concentrated level of the TFR slice.

To adaptively select the angle that matches the frequency of the windowed signal from the string of discrete angles α, the index kurtosis—which can measure the energy concentration level at a given instant in time—is proposed for use. The discrete angles are defined as [23]

$$a_i = -\frac{\pi}{2} + \frac{i}{N+1}\pi, \quad i = 1, 2, \ldots, N \qquad (3)$$

where N is the number of discrete angles and the range of the inclination angle α is $(-\pi/2,\ \pi/)$. It is worth mentioning that, theoretically, the larger the value of N, the more accurate the selected angles should be. However, a large value of N will increase computational complexity. Therefore, it is recommended to reach a compromise between increasing the value of N and the computing time when improving accuracy. When $N = 1$ and $\alpha = 0$, the kernel in (1) is identical to the one of the STFT, indicating that the STFT is a special case of the proposed MLCT. Among the N discrete angles, the one that can correctly reflect the actual frequency of the windowed signal can be selected with the guidance of kurtosis, expressed as

$$\hat{\alpha} = \underset{\alpha_i, i=1,2,\ldots,N}{\arg\max} \left(kurt\left(S_{\alpha_i}(u,\omega) \right) \right) \qquad (4)$$

where *kurt*( ) denotes the operation of calculating the kurtosis of the TFR slice obtained by the ith angle. For a signal segment within a short window, the frequency that can be also represented by an inclination angle is adaptively determined using (4). As stated previously, the true inclination angle corresponds to the highest level of energy concentration; thus, the selected angle corresponds to the maximum kurtosis. Sliding the window until the entire signal is involved, the final TFR of the signal is a combination of the TFR slices corresponding to each maximum value of kurtosis, recorded as $S_{\hat{\alpha}}(u,\omega)$. Using the proposed matching linear chirplet strategy, the TFR of the signal can be enhanced without pre-estimation of the IF.

B. BRIEF INTRODUCTION OF SET

It can be seen that, by matching the chirp rate of the analyzed signal under the guidance of kurtosis, the TFR obtained in subsection II. A has been enhanced. However, further improvements can be made.

SET is a powerful TFR post-processing tool that employs a defined extracting operator similar to the impulse function. The purpose of applying SET is to extract the TF distributions around the target frequency [24], expressed as

$$S^E(u,\omega) = \int_{-\infty}^{+\infty} S(u,\omega) \cdot \delta\left(\omega - \omega(u,\omega)\right) \mathrm{d}\omega \qquad (5)$$

where $\omega(u,\omega)$ is the IF estimator [3], [17] and $\delta(\ )$ is the impulse function, which can be calculated by their definitions, respectively formulated as

$$\omega(u,\omega) = \frac{\partial_u S(u,\omega)}{S(u,\omega)} = \omega + i\frac{S^{g'}(u,\omega)}{S(u,\omega)} \qquad (6)$$

$$\delta\left(\omega - \omega(u,\omega)\right) = \begin{cases} 1, & \omega = \omega(u,\omega) \\ 0, & \omega \neq \omega(u,\omega) \end{cases} \qquad (7)$$

It can be seen that SET has the same formulation as SST. The main difference between these two post-processing techniques is the implementation of the impulse function. SST has been developed to redistribute the TFR along the frequency axis through the guidance of the IF estimator. Similarly, the final result of SET also depends on the same IF estimator as that in (6); however, the reassignment operations in the SST are replaced by extracting operations in SET.

With SET, only the TF distributions related to frequency components of interest in the signal are restored and the others are removed by the extracting operator. It is obvious that SET can obtain sharper IF ridges than STFT. However, even though SET can sharpen the IF ridges in the TFR, the energy concentration level of the TFR after SET is unchanged, limiting its applicability to incipient fault detection. Therefore, the integration of the proposed matching linear chirplet strategy and the extracting operation could address such problems, as the former can concentrate the energy level and the latter is capable of further sharpening the TFR.

C. PROPOSED MLCSET

Supposing that the angle is accurately selected for increasing the TF energy concentration level and the IF estimator matches the true IF, the TFR of MLCSET can be defined as

$$S^E_{\hat{\alpha}}(u,\omega) = S_{\hat{\alpha}}(u,\omega) \cdot \delta\left(\omega - \tilde{\omega}(u,\omega)\right) \qquad (8)$$

where the $\tilde{\omega}(u,\omega)$ is the IF estimator. According to (6), it can be formulated as

$$\begin{aligned}\tilde{\omega}(u,\omega) &= \frac{\partial_u S_{\hat{\alpha}}(u,\omega)}{jS_{\hat{\alpha}}(u,\omega)} \\ &= \omega + j\frac{S_{\hat{\alpha}}^{g'}(u,\omega)}{S_{\hat{\alpha}}(u,\omega)} + \omega\tan\hat{\alpha}(u)\frac{S_{\hat{\alpha}}^{tg}(u,\omega)}{S_{\hat{\alpha}}(u,\omega)} \\ &\quad + o\left(\tan\left(\hat{\alpha}(u)'\right)\right) \end{aligned} \tag{9}$$

where $\hat{\alpha}(u)$ is constant and $\left(\hat{\alpha}(u)\right)' = 0$. Note that $\omega\tan\hat{\alpha}(u) = \omega'$ is determined by changes in the frequency component and reflects the chirp-rate of the signal at time instant $t = u$ [22]. The TFRs $S_{\hat{\alpha}}^{g'}(u,\omega)$ and $S_{\hat{\alpha}}^{tg}(u,\omega)$ are obtained with window $g'(t)$ and $tg(t)$, and satisfy [28]

$$\tilde{t}(u,\omega) = u - \frac{S^{tg}(u,\omega)}{S(u,\omega)} \tag{10}$$

where $\tilde{t}(u,\omega)$ is the group delay estimator. Therefore, if no group delay is taken into consideration, i.e., $\tilde{t}(u,\omega) = u$, the IF estimator in (9) can be further simplified as

$$\tilde{\omega}(u,\omega) = \omega + j\frac{S_{\hat{\alpha}}^{g'}(u,\omega)}{S_{\hat{\alpha}}(u,\omega)} \tag{11}$$

which is echoed with the IF estimator in (6).

Then, the implementation of the simplified IF estimator in (11) can be derived as

$$\delta(\omega - \tilde{\omega}(u,\omega)) = \begin{cases} 1, & j\dfrac{S_{\hat{\alpha}}^{g'}(u,\omega)}{S_{\hat{\alpha}}(u,\omega)} = 0 \\ 0, & j\dfrac{S_{\hat{\alpha}}^{g'}(u,\omega)}{S_{\hat{\alpha}}(u,\omega)} \neq 0 \end{cases} \tag{12}$$

However, considering the calculation error and that the real part of the IF estimator should be used in practice, (12) is rewritten as

$$\delta(\omega - \tilde{\omega}(u,\omega)) = \begin{cases} 1, & \left|\mathrm{Re}\left(j\dfrac{S_{\hat{\alpha}}^{g'}(u,\omega)}{S_{\hat{\alpha}}(u,\omega)}\right)\right| < \dfrac{\Delta\omega}{2} \\ 0, & \left|\mathrm{Re}\left(j\dfrac{S_{\hat{\alpha}}^{g'}(u,\omega)}{S_{\hat{\alpha}}(u,\omega)}\right)\right| \geq \dfrac{\Delta\omega}{2} \end{cases} \tag{13}$$

where $\Delta\omega$ is the frequency resolution and Re( ) denotes the function that accepts only the real part.

As an important indicator to evaluate the TFA method, the signal reconstruction of the proposed MLCSET is also conducted

$$\begin{aligned}&\int_{-\infty}^{+\infty} S_{\hat{\alpha}}^{E}(u,\omega)\,\mathrm{d}\omega \\ &= \int_{-\infty}^{+\infty} S_{\hat{\alpha}}(u,\omega)\int_{-\infty}^{+\infty}\delta(\eta - \tilde{\omega}(u,\omega))\,\mathrm{d}\eta\mathrm{d}\omega \\ &= \int_{-\infty}^{+\infty} S_{\hat{\alpha}}(u,\omega)\,\mathrm{d}\omega \\ &= \int_{-\infty}^{+\infty} s(t+u)\,g(t)\int_{-\infty}^{+\infty} e^{-j\omega\left(t+0.5\tan\hat{\alpha}(u)t^2\right)}\mathrm{d}\omega\mathrm{d}t \\ &= \int_{-\infty}^{+\infty} s(t+u)\,g(t)\,2\pi\delta\left(t+0.5\tan\hat{\alpha}(u)\,t^2\right)\mathrm{d}t \\ &= 2\pi g(0)\,s(u) \end{aligned} \tag{14}$$

where $\delta(\,)$, as defined above, denotes the impulse function and $g(0)$ is a constant determined by the window function. It can be found that when $t = 0$, the original signal waveform $s(u)$ in the time domain can be reconstructed from the TFR obtained using the proposed method.

The algorithm implementation of the discrete MLCSET is illustrated as follows. The discrete data is denoted by $x[l]$, $l = 0, 1, \ldots, L-1$, where L is the length of samples. The data $x[l]$ corresponds to a uniform discretization of $x(t)$ taken at time $t_n = t_0 + lT$, where T is the sampling interval. The discrete TFR of the matching chirp-rate strategy can be calculated as

$$\begin{aligned}&S_{\alpha_i}[n_t, n_f] \\ &= \sum_{l=0}^{L-1} x[l]\,g[l-n_t]\,e^{-j\frac{2\pi}{N}n_f\left([l-n_t]+\frac{\tan\alpha_i(n_t)}{2}[l-n_t]^2\right)}, \\ &\quad i = 1, 2, \ldots, N_\alpha \end{aligned} \tag{15}$$

where N_α is the number of the discrete angles used in the matching strategy.

The selected TFR slice at time instant $t = n_t$ is recorded as $S_{\hat{\alpha}}[n_t, n_f]$. Then the IF estimator is obtained as

$$\tilde{\omega}[n_t, n_f] = \begin{cases} \mathrm{Ro}\left[n_f + \mathrm{Re}\left[\dfrac{j}{2\pi}\cdot\dfrac{L}{L_{win}}\cdot\dfrac{S_{\hat{\alpha}}^{g'}[n_t, n_f]}{S_{\hat{\alpha}}[n_t, n_f]}\right]\right], \\ \qquad\qquad if\ S_{\hat{\alpha}}[n_t, n_f] \neq 0 \\ 0, \\ \qquad\qquad if\ S_{\hat{\alpha}}[n_t, n_f] = 0 \end{cases} \tag{16}$$

where Ro[ ] denotes using a round operation, making the default resolution of the discrete IF estimator in (16) be $\Delta\omega = 1$. $S_{\hat{\alpha}}^{g'}[n_t, n_f]$ is the corresponding TFR obtained by using the first derivative of window g'(), L is the length of samples, and L_{win} is the length of the window used to truncate the discrete samples. L/L_{win} can be considered to be the coefficient to expand the frequency segment to satisfy the requirement for a Fourier transform. The discrete MLCSET can then be written as

$$S_{\hat{\alpha}}^{E}[n_t, \xi] = \sum_{n_f=0}^{L-1} S_{\hat{\alpha}}[n_t, n_f]\,\delta\left[\xi - \tilde{\omega}[n_t, n_f]\right] \tag{17}$$

The pseudocode of the proposed method can be found in Algorithm 1. A flowchart of the proposed method is also shown in Figure 1.

III. SIMULATION STUDY

In this section, the proposed method is analyzed using numerical data and comparisons made between different TFA methods.

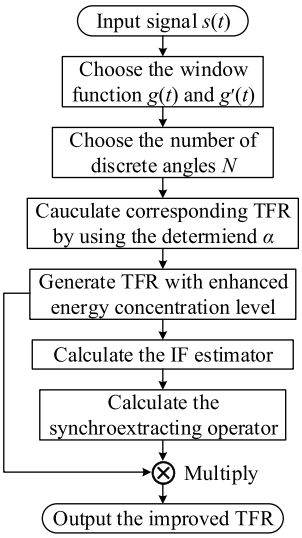

FIGURE 1. Flowchart of the proposed method.

A multi-component signal $s(t)$ with time-varying IFs can be defined as

$$s(t) = \sum_{i=1}^{2} \sin\left(k_i \int_0^4 2\pi f(t)\,\mathrm{d}t\right), \times f(t) = 20e^{-1.2(t-1.2)^2} + 15 \quad (18)$$

where k_i is (1,2), respectively, for $i = 1,2$ and $f(t)$ is the IF. The noise-free and noisy versions of the multi-component signals are analyzed. The sampling frequency of the simulated signal is set to 200 Hz and the signal lasts for 4 s. The noise-free signal waveform and the frequency trajectories are shown in Figure 2 (a) and (b), respectively.

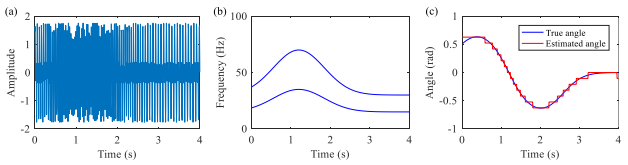

FIGURE 2. Noise-free simulation signal: (a) simulated noise-free waveform, (b) frequency trajectories of the simulated signal, and (c) angle (blue: true; red: estimated).

The selected angles, guided by the proposed chirp-rate matching strategy, are shown in Figure 2 (c), where the true angles and selected angles are plotted using solid blue and red lines, respectively. It can be seen that the selected angles match the true ones well. The improved TFR provided by the proposed MLCT is shown in Figure 3 (b) and the STFT result is plotted in Figure 3 (a), for comparison. It can be seen that the TFR obtained by the proposed MLCT is more energy-concentrated than the one obtained by STFT. In addition to the traditional STFT, other TFA methods, such as wavelet transform (WT), along with post-processing techniques like SST are also used to analyze the simulated signal. The resulting TFRs are shown in Figure 3 (c) and (d). It can be observed that the TFRs of the two methods suffer from TF blurriness,

Algorithm 1 Proposed MLCSET

Step 1: *Initialization and calculation*
Choose the window function g and the number of discrete angles N;
Calculate the discrete window g';
Calculate the discrete angles α_i, $i = 1, 2, \ldots, N$;
Step 2: Enhance TFR by matching strategy
for $i = 1{:}\,N$
Calculate $S_{\alpha_i}[u,\omega]$ and $S_{\alpha_i}^{g'}[u,\omega]$;
end
Find $S_{\hat{\alpha}}[u,\omega] \leftarrow \arg\max_{\alpha_i}\left(kurt\left(S_{\alpha_i}[u,\omega]\right)\right)$ according to (4);
Step 3: *Synchroextracting*
Choose the threshold γ, $\Delta\omega$;
$IF[nt, nf] \leftarrow 0$;
Calculate $\tilde{\omega}(nt, nf)$ according to (16);
for $nt = 1{:}\,t$ bins
for $nf = 1{:}\,f$ bins
if $abs\left(S_{\hat{\alpha}}[nt, nf]\right) > \gamma$
if $abs\left(real\left(\omega - \tilde{\omega}(nt, nf)\right)\right) < \Delta\omega/2$
$IF[nt, nf] \leftarrow 1$;
end if
end if
end for
end for
Step 4: Calculate MLCSET
$S_{\hat{\alpha}}^{E}(u,\omega) = S_{\hat{\alpha}}(u,\omega) \cdot IF(u,\omega)$;
Output $S_{\hat{\alpha}}^{E}(u,\omega)$;

particularly for signal segments with rapidly changing IFs. The conventional STFT-based SET is also applied to the simulated signal, as shown in Figure 3 (e). We can discern that the IF ridges are sharpened; however, the IF ridge segments from 0–1 s and 1.5–2.5 s still suffer from the blurriness since the original TFR segments from the STFT experience smearing and the SET is incapable of improving the energy concentration level.

Then, the proposed method is used for simulated signal processing. The TFR generated by the proposed MLCSET is shown in Figure 3 (f). As mentioned before, applying the SET can be regarded as extracting the TF distributions around the true IF from the original TFR, leading to more sharpened IF ridges and less TF diffusion. It can be clearly seen that the TFR in Figure 3 (f) has sharper IF ridges and does not suffer from smearing problems. The proposed MLCSET could further increase the readability of the TFR by enhancing the original TFR and multiplying a more accurate extracting operator. For this simulated signal, the window length for analysis was set as 0.8 s. By reaching a compromise between the TFR readability and computing time, the number of angles N is set 30. Further increasing the value of N did not lead to a substantial TFR improvement, but did increase computational complexity.

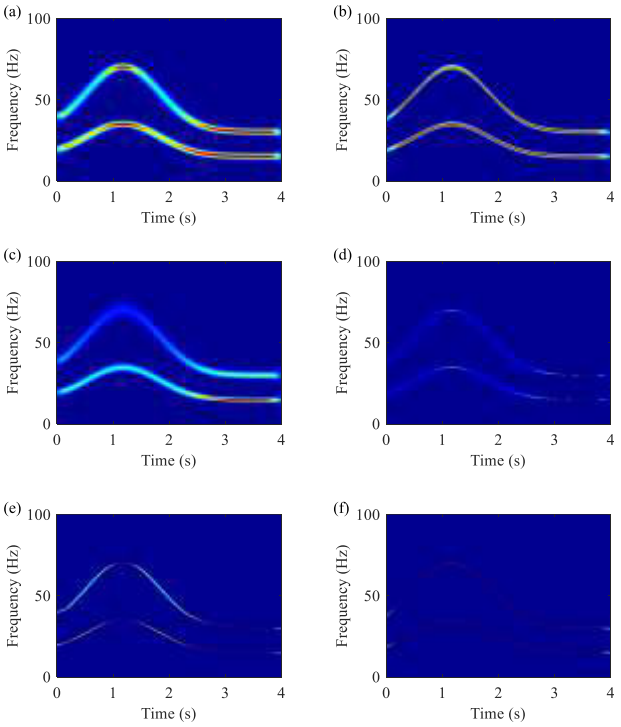

FIGURE 3. Time-frequency representations when using different methods for the noise-free simulation signal: (a) analyzing result using STFT, (b) analyzing result using MLCT method, (c) analyzing result using WT, (d) analyzing result using SST, (e) analyzing result using STFT-based SET, and (f) analyzing result using MLCSET.

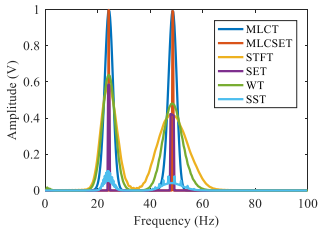

FIGURE 4. Spectrum slices of the noise-free signal at the time instant t = 2s using different methods.

To better illustrate the improvement in TFR energy concentration level by the proposed MLCSET method, the TFR slice at time instant $t = 2$ s—which reflects the energy concentration level at that time instant—is plotted in Figure 4 (red line). Similarly, the TFR slices at time instant $t = 2$ s of other TFA methods mentioned in Figure 3 are also analyzed. The comparison result is shown in Figure 4. It can be seen that the proposed MLCT and MLCSET have the highest TF amplitudes, indicating that the TFR energy concentration level can be increased by the proposed chirp-rate matching strategy. Figure 4 also shows that the amplitude of MLCT and MLCSET at the time instant is identical, which means that SET does not improve the energy concentration level but extracts the original TF distributions around the true IFs (the TFR slice of MLCSET is much narrower than that of MLCT), i.e., the MLCSET only extracts several frequency bins around the true IFs from the TFR by MLCT. The same is true for STFT and SET.

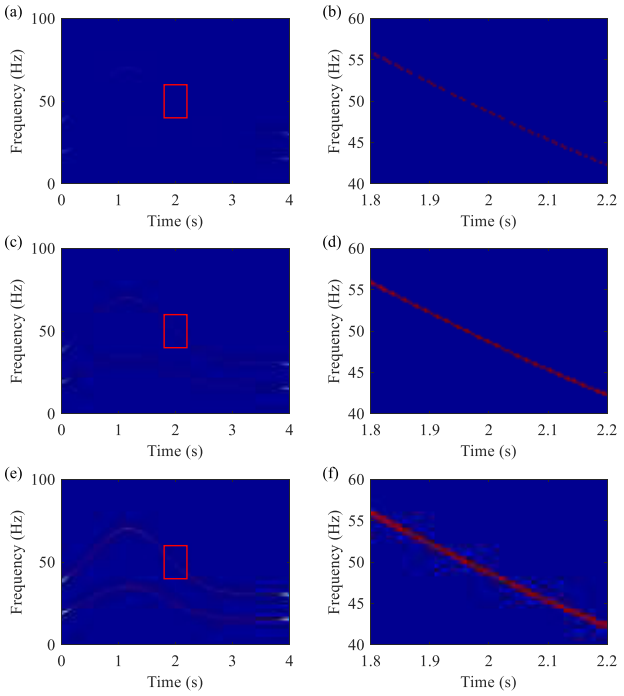

FIGURE 5. Results obtained for differing values of $\Delta\omega$ with corresponding local zooms on the right: (a) time–frequency representation when $\Delta\omega = 0.5$, (b) local zoom of the result when $\Delta\omega = 0.5$, (c) time–frequency representation when $\Delta\omega = 1$, (d) local zoom of the result when $\Delta\omega = 1$, (e) time-frequency representation when $\Delta\omega = 2$, (f) local zoom of the result when $\Delta\omega = 2$.

The parameter $\Delta\omega$, used in Algorithm 1, takes the frequency resolution into account and can be considered to be a threshold that determines the number of the extracted frequency bins via SET. Usually, setting $\Delta\omega = 1$ can satisfy the requirements of extracting the TF distributions around the true IF only if the window length is appropriately selected for analysis. For demonstration purposes, in this study, the value of parameter $\Delta\omega$ is set as 0.5, 1, and 2, and the corresponding results are shown in Figure 5 (a)–(f), with their local zooms (marked in red rectangles) in the right column.

It can be seen from Figure 5 (a)–(b) that the IF trajectory is sharper, but some TF distributions (0–1 frequency bin at time instant $t = 2$ s) are missed for $\Delta\omega = 0.5$. In comparison to Figure 5 (e)–(f), where the parameter $\Delta\omega$ is set 2, TF distributions in a wider frequency range (covering 2 or 3 frequency bins) are retained, leading to wider IF trajectories. The results for $\Delta\omega = 1$ are given in Figure 5 (c)–(d). The corresponding IF ridges occupy 1 or 2 frequency bins at the given time instant, which are less than those when $\Delta\omega = 2$. More importantly, no TF details are missed. Considering that the frequency resolution is constant and $\Delta\omega$ determines how many frequency bins are retained, it is suggested that the parameter $\Delta\omega$ should be tuned to generate a satisfactory TFR (locating only one frequency bin at a given time instant) that does not lose detailed time-varying features.

To facilitate a more in-depth understanding, the amplitudes of TFR slices within the frequency range of 20–55 Hz at time instant $t = 2$ s are plotted in Figure 6. It can be seen

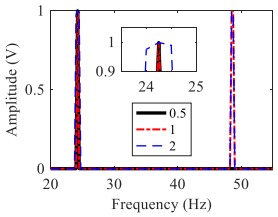

FIGURE 6. Spectrum slices for different values of $\Delta\omega$ (black: 0.5; red: 1; blue: 2).

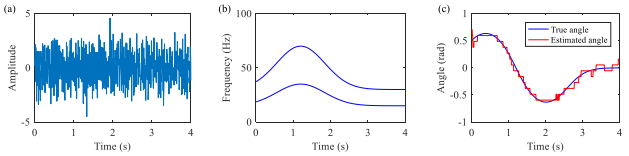

FIGURE 7. Noisy simulated signal: (a) noisy signal waveform, (b) IF trajectories of the simulated signal, (c) angles (blue: true; red: estimated).

that a value of $\Delta\omega = 0.5$ fails to distinguish the target frequency around 50 Hz. The value of $\Delta\omega = 1$ occupies a certain frequency bin for the lower frequency component (between 24–25 Hz) and the value of $\Delta\omega = 2$ covers more frequency bins, as shown in the local zoom in Figure 6. The detailed analyses further illustrate that a larger value of $\Delta\omega$ will not omit any target TF details; however, it results in wider frequency trajectories. A very small value of $\Delta\omega$ will generate sharp IF trajectories, but it may omit some useful details. Therefore, it is suggested that $\Delta\omega$ be set as 1. During practical use, users can slightly vary this parameter to obtain a satisfactory TFR, according their intended application.

The noisy signal, with a signal-to-noise ratio (SNR) of 0 dB, is then analyzed to further test the performance of the proposed method. The noisy signal's waveform is plotted in Figure 7 (a). The frequency trajectories are shown in Figure 7 (b).

The angle for the noisy signal is also estimated using the guidance of kurtosis, as shown in Figure 7 (c). It can be observed that, even though slight oscillations are present because of noise, the selected angles and true ones match well. The slight deviations between the selected angles and true angles have a negligible effect on the TFR readability, as shown in Figure 8 (b).

The TFRs obtained using STFT and the proposed MLCT are shown in Figure 8 (a) and (b). The TFR in Figure 8 (a) suffers from severe smearing. The TFR of MLCT can reveal the IFs of signal components; however, the IF ridges are not sharp enough and are blurry at some instances in time, such as $t = 2$ s. The TFRs obtained from the WT, SST, and SET—in Figure 8 (c)–(e)—all suffer from smearing; therefore, it is difficult to accurately recognize the IF ridges, particularly at 0–3 s. The result obtained using the proposed MLCSET is presented in Figure 8 (f), where it can be seen that the energy concentration level is improved and the IF ridges are much sharper. Then, the IF can be accurately extracted from this improved TFR and used for rotating machinery fault diagnosis.

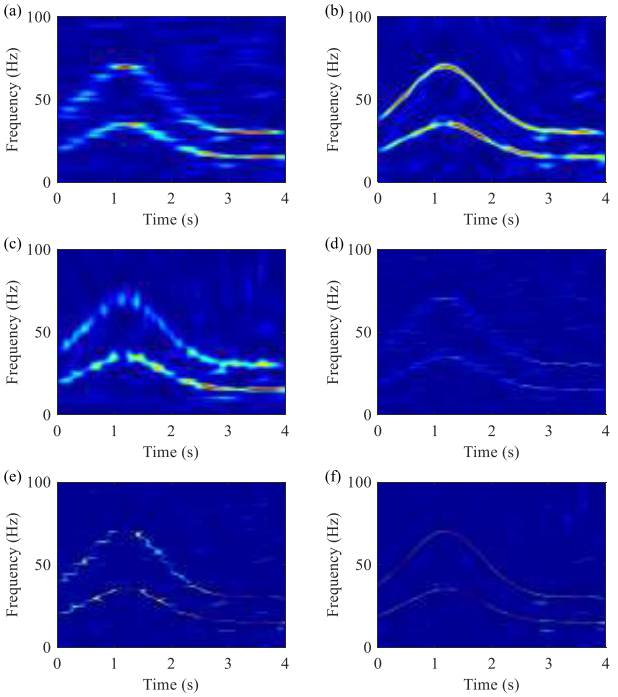

FIGURE 8. Noisy simulation signal analysis using different methods: (a) analyzing result using STFT, (b) analyzing result using MLCT, (c) analyzing result using WT, (d) analyzing result using SST, (e) analyzing result using STFT-based SET, and (f) analyzing result using MLCSET.

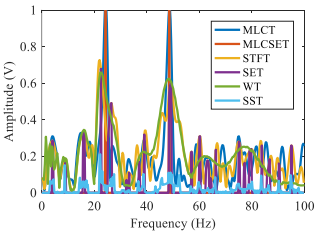

FIGURE 9. Spectrum slices of the noisy simulated signal at the time instant t = 2s using different methods.

Similar to the noise-free simulated signal, the amplitudes of the TFR slices at time instant $t = 2$ s for different TFA methods are analyzed, as shown in Figure 9. Figure 9 clearly shows the amplitudes of the TFR slices of MLCT and MLCSET. Moreover, the amplitude of the TFR slice of MLCSET is further shifted towards the target frequency, in comparison to the result from MLCT. These observations indicate that the proposed methods can yield the TFR with the sharpest IF ridge and highest energy concentration level. It is worth noting that, in comparison to Figure 4, there are more fluctuations present in Figure 9 owing to noise.

To evaluate the performance of the proposed method, Rényi Entropy is used. For TFR $S(u, \omega)$, the Rényi Entropy can be calculated as follows

$$R_S = \frac{1}{1-\alpha}\log_2 \times \iint \left(S(u,\omega) \Big/ \iint S(u,\omega)\, du d\omega \right)^{\alpha} du d\omega \quad (19)$$

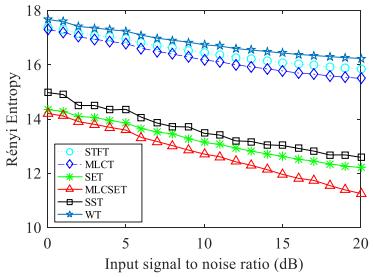

FIGURE 10. Rényi entropy versus the signal to noise ratio of the input signal.

TABLE 1. Rényi entropy of the analyzed signal by different methods.

TFA method	WT	STFT	MLCT	SST	SET	MLCSET
Noise-free	15.99	15.56	15.12	12.15	11.93	10.94
SNR=0 dB	17.67	17.42	17.31	15.05	14.42	14.26

where α denotes the rank, which is selected to be 3 here. It can be seen from Table 1 that employing post-processing techniques such as SET can further decrease the Rényi Entropy. The proposed MLCSET has the lowest Rényi Entropy for both noise-free and noisy cases. To further understanding the capability of the different TFA methods to mitigate noise, the Rényi Entropy versus SNRs of the input signals are analyzed. The SNR varies from 0–20 dB and the results are given in Figure 10. It can be concluded that the proposed MLCSET outperforms other TFA methods in terms of resilience to noise.

IV. APPLICATION TO ROTATING MACHINERY FAULT DIAGNOSIS UNDER VARIABLE SPEED CONDITIONS

In this section, a simulated bearing signal and two experimental signals under time-varying speed conditions are analyzed to validate the proposed method. In addition to the improved TFR energy concentration level, the accuracies of the detected IF ridges are also analyzed in this section to evaluate the health condition of the rotating machinery. For bearing-fault diagnosis, the ratios of the extracted fault-related IF ridges to the extracted shaft-related IF ridges should be calculated. Then, the fault type can be determined according to the average ratios of the extracted IF ridges. In gears, the main feature related to faults in vibration signals is the modulation effect, i.e., the signal component of meshing is modulated by the gear fault characteristic frequency. If the sidebands of the meshing frequency can be observed on the TFR, it then can be concluded that the gear is defective. The fault-diagnosis strategy of rotating machinery can be summarized as: (1) acquiring the TFR, (2) performing IF-ridge extraction based on the obtained TFR, and (3) diagnosing the fault type based on the extracted IF ridges.

A. SIMULATED BEARING SIGNAL ANALYSIS

To exam the effectiveness of the proposed MLCSET in diagnosing bearing faults, a simulated vibration signal is first constructed. The sampling frequency is set to 8000 Hz and the signal lasts for 1 s. The instantaneous shaft rotation frequency f_{ISRF} first increases, then decreases, and finally stabilizes at a constant value. The simulated signal $x(t)$ is defined as

$$\begin{aligned} x(t) &= \sum_{i=1}^{L} A_i e^{-\beta(t-t_i)} \sin(2\pi f_r t) \\ &\quad + \sum_{j=1}^{3} R_j \cos\left(2\pi m f_{\mathrm{ISRF}} t + \varphi_j\right) + n(t) \\ f_{\mathrm{ISRF}} &= 40e^{-1.2(4t-1)^2} + 30,\ \beta = 1000,\ f_r = 3500, \\ R_1 &= 0.2, R_2 = 0.15, R_3 = 0.1;\ \varphi_1 = \frac{\pi}{6}, \\ \varphi_2 &= -\frac{\pi}{3}, \varphi_3 = \frac{\pi}{2}, \end{aligned} \tag{20}$$

where A_i and t_i represent the time-varying amplitude and occurrence time of the ith impulse, respectively. The length of this simulated bearing signal is L. β is the damping parameter and f_r is the resonance frequency. The first term of (20) is a series of impulses generated by a local defect in a bearing. The second term denotes the components from the shaft, where f_{ISRF} is the instantaneous shaft rotating frequency. R_j and φ_j represent the amplitude and initial phase of the jth harmonic ($j = 1, 2, 3$), respectively. The final term, $n(t)$, represents noise.

The ratio of the instantaneous fault characteristic frequency f_{IFCF} to the instantaneous shaft rotation frequency f_{ISRF} is referred to as the fault characteristic coefficient (FCC), which is time-invariant with the shaft rotating speed and can, therefore, be used for bearing-fault diagnosis. It is set as 2.7 for the simulated signal, indicating that the instantaneous fault characteristic frequency $f_{\mathrm{IFCF}} = 2.7 f_{\mathrm{ISRF}}$.

The SNR of this simulated bearing signal is set as 6 dB. The noisy signal waveform and estimated angles selected using maximal kurtosis are plotted in Figure 11 (a) and (b), respectively. Even if the estimated angles slightly deviate from the true ones at some time instants, in general, the estimated angles match the true ones well—as shown in Figure 11 (b)—under the guidance of kurtosis. These estimated angles enable the proposed method to enhance the TFR without IF information.

The simulated signal is first processed using STFT and the resulting TFR is shown in Figure 12 (a), which indicates the presence of smearing problems. Figure 12 (b) shows the TFR obtained using MLCT. The readability of the TFR generated

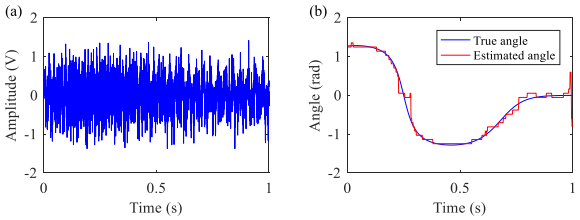

FIGURE 11. Noisy simulated bearing signal: (a) noisy waveform of the simulated bearing signal, (b) estimated angles and ture angles (blue: true; red: estimated).

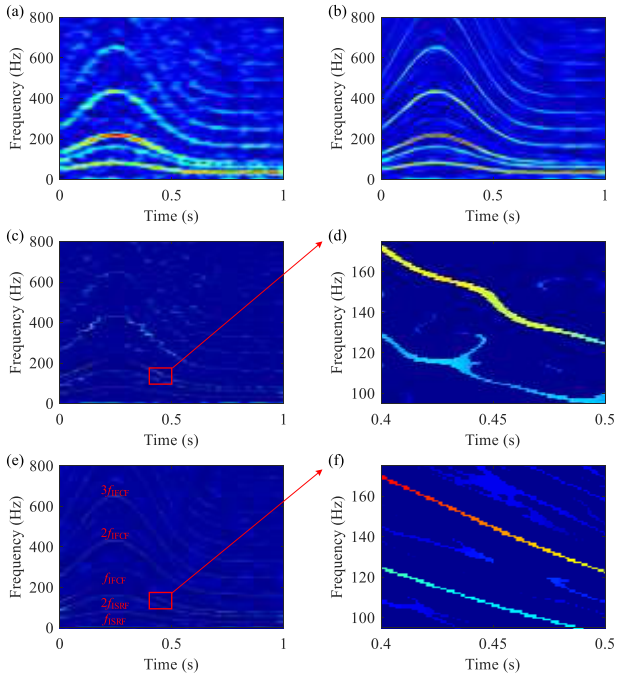

FIGURE 12. TFRs of noisy simulated bearing signal: (a) analyzing result using STFT, (b) analyzing result using MLCT, (c) analyzing result using STFT-based SET, (d) analyzing result using MLCSET, (e) local zoom of STFT-based SET, (f) local zoom of MLCSET.

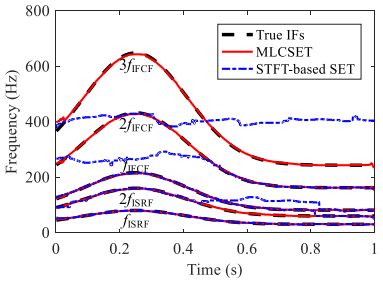

FIGURE 13. Detected IF ridges of simulated noisy signal (black: true; red: propsoed MLCSET; blue: STFT-based SET).

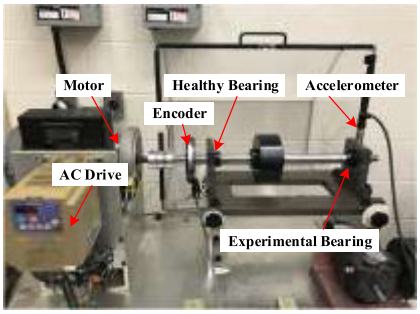

FIGURE 14. Bearing fault experimental set-up.

by MLCT is much improved, in comparison to the result of STFT. Five IF trajectories can be clearly distinguished in Figure 12 (b), including f_{ISRF}, f_{IFCF}, and their harmonics. Next, the SET operation is performed. The STFT-based SET and MLCSET results are given in Figure 12 (c) and (e), with their local zooms shown in Figure 12 (d) and (f), respectively. It is clear that the TFR in Figure 12 (e) better represents the IF trajectories than the TFR in Figure 12 (c). More detailed comparisons can be found in Figure 12 (d) and (f). Specifically, the IF ridges in Figure 12 (f) are sharper and more energy-concentrated.

The improved TFR obtained using the proposed method can lead to a more accurate IF extraction. The extracted IF ridges are shown in Figure 13, indicating that the IFs (red solid lines) are accurately extracted from the TFR of the proposed MLCSET. The IFs extracted from the TFR of the STFT-based SET (blue dashed lines) cannot correctly reflect the varying pattern of true IFs. It can then be concluded that the proposed method improves the readability of TFRs and facilitates the extraction of IF ridges for bearing-fault diagnosis.

B. APPLICATION TO BEARING INNER RACE FAULT DIAGNOSIS

In this subsection, the proposed MLCSET is applied to process vibration signals collected from a bearing with an inner race fault. Then, the detection of IF ridges is attempted from the MLCSET-resulting TFR for diagnosing the bearing-fault type under time-varying speed conditions.

The vibration signal is collected using the experimental setup shown in Figure 14. The experiments are conducted using the SpectraQuest machinery fault simulator (MFS-PK5M), which holds two ER16K ball bearings and the bearing on the right side has an inner race fault. The shaft is powered by an AC drive. An accelerometer is mounted to record the vibration data and an encoder (EPC model 775) is used to measure the instantaneous shaft rotating frequency f_{ISRF}, which is obtained for validation purposes. The specifications of the bearing with the inner race fault are given in Table 2. The FCC is calculated to be 5.43, which means that $f_{\mathrm{IFCF}} = 5.43 f_{\mathrm{ISRF}}$.

TABLE 2. Bearing parameters.

Bearing type	Pitch diameter	Ball diameter	Number of balls	FCC
ER16K	38.52 mm	7.94 mm	9	5.43

The signal waveform is illustrated in Figure 15 (a). The shaft rotation frequency decreases from 25 Hz to 15 Hz and then goes back to 20 Hz in Figure 15 (b). The selected angles with the guidance of kurtosis are shown in Figure 15 (c), which match the true angles, indicating that the angles are accurately selected for the implementation of the proposed MLCSET.

The TFRs obtained using different TFA methods are shown in Figure 16 (a)-(d), with the local zooms of TFR segments marked by red rectangles. The rows in Figure 16 correspond to the processing results of STFT, MLCT, STFT-based SET, and MLCSET. The column in the left represents the TFRs obtained using the four different TFA methods and the columns in the middle and on the right display

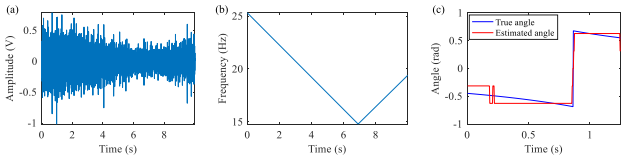

FIGURE 15. Experimental bearing vibration signal: (a) vibration signal waveform, (b) shaft rotational frequency,(c) estimated angles (blue: true; red estimated).

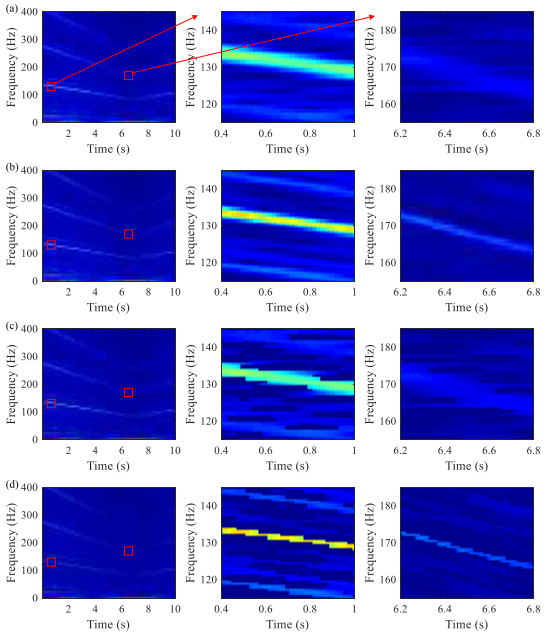

FIGURE 16. Analysis results of the experimental bearing signal and local zooms on the right: (a) analyzing results using STFT, (b) analyzing results using MLCT, (c) analyzing results using STFT-based SET, (d) analyzing results using MLCSET.

the local zooms of the TFR segments, marked by red rectangles. It can be observed that rough IF sketches can be revealed by all the mentioned TFA methods in this case. However, through close observations using local zooms, one can easily see that MLCT (Figure 16 (b)) can enhance the energy concentration level on TFRs in comparison to STFT (Figure 16 (a)). Subsequently, when integrated with the SET operation, the IF ridges on the TFR can be further sharpened, as shown in Figure 16 (d). Figure 16 (c) shows the TFR and local zooms of the original SET (i.e., STFT-based SET), where the IF ridges are not as concentrated as the ones in Figure 16 (d). The comparisons show that the proposed MLCSET can improve the TFR readability and yield the TFRs with the sharpest IF trajectories.

The IFs extracted from the MLCSET-generating TFR are shown in Figure 17. The true IFs and IFs extracted from the original SET-resulting TFR are also shown in Figure 17 to facilitate comparison. It is clear that the TFR of MLCSET successfully reveals the IF ridges of the signal, from which the IFs can be accurately extracted. Nevertheless, IFs in the lower frequency band cannot be extracted from the TFR of STFT. To quantitatively evaluate the accuracy of the detected IF ridges, the mean relative errors (MREs) of extracted IF ridges

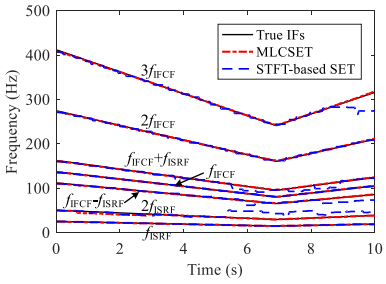

FIGURE 17. Detected IF ridges of the experimental bearing signal (black: true; red: proposed MLCSET; blue: SET).

TABLE 3. MREs of detected IF ridges and average ratios of the detected (true) f_{IFCF} and its harmonics to the detected (true) f_{ISRF}.

Extracted IF ridges Ratios and MREs		f_{ISRF}	$2f_{ISRF}$	f_{IFCF}	$2f_{IFCF}$	$3f_{IFCF}$	f_{IFCF}-f_{ISRF}	f_{IFCF}+f_{ISRF}
True ratios		1	2	5.43	10.86	16.29	4.43	6.43
MLCSET	Average ratios	1	1.970	5.433	10.887	16.331	4.438	6.444
	MREs	1.17%	2.25%	0.3%	0.26%	0.24%	0.39%	0.3%
STFT-based SET	Average ratios	1	2.327	5.428	10.844	16.122	4.309	6.269
	MREs	1.13%	19.6%	3.34%	0.59%	1.49%	3.34%	0.28%

(Note: In Table **3**, the true ratios are the ratios of true IFCF and its harmonics to measured f_{ISRF}, and the average ratios represent the ratios between the extracted f_{IFCF} and its harmonic to the extracted f_{ISRF}.).

are calculated in Table 3. The average ratios of the extracted f_{IFCF} and its harmonics to the extracted f_{ISRF} are also calculated, as shown in Table 3, for the fault-type diagnosis. The ratios of the actual f_{IFCF} ($= 5.43 f_{ISRF}$) and its harmonics to the measured f_{ISRF} are also given in Table 3, for comparison. The MREs of the extracted IF ridges of MLCSET are far less than 5%; however, the MREs of extracted IF ridges of STFT-based SET are much higher than the ones in MLCSET (as high as 19.6%), indicating that the proposed method could improve TFR readability and ensure that accurate IF ridges are extracted.

The average ratio of the extracted f_{IFCF} to f_{ISRF} is 5.433, as shown in Table 3, which is identical to the actual ratio (5.43), calculated according to the bearing type and its specifications, listed in Table 2. The average ratios of the second and third harmonics of extracted f_{IFCF}—i.e., $2f_{IFCF}$ and $3f_{IFCF}$– to f_{ISRF} are also given in Table 3, which respectively equal to 2FCC (10.86) and 3FCC (16.29). In addition, there are sidebands around the instantaneous fault characteristic frequency. The average ratios of f_{IFCF}-f_{ISRF} and $f_{IFCF} + f_{ISRF}$ to f_{ISRF} coincide with the actual values as well. It can then be concluded that there is an inner race fault on the bearing, which is consistent with the test setup.

C. APPLICATION TO HEALTHY PLANETARY GEARBOX

To further analyze the proposed method, it is used to process data collected from a healthy planetary gearbox. The experimental setup is shown in Figure 18.

The specifications of the planetary gearbox used in this experiment are given in Table 4. The experiment operates

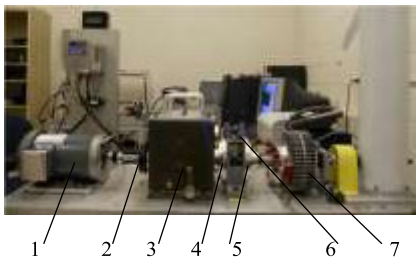

FIGURE 18. Planetary gearbox test rig (1: Motor; 2: Tachometer; 3: Fixed-shaft gearbox; 4: Planetary gearbox stage 1; 5: Planetary gearbox stage 2; 6: Accelerometer; 7: Brake).

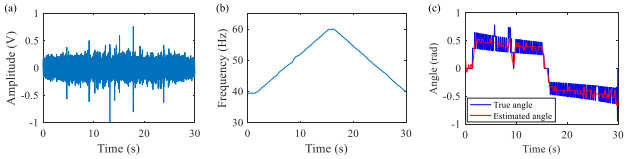

FIGURE 19. The planetary gearbox signal: (a) planatery vibration signal waveform, (b) shaft rotation speed, (c) estimated angles and true angles (blue: true; red: estimated).

TABLE 4. Parameters of the planetary gearbox.

Gear type	Number of gear teeth	
	Stage 1	Stage 2
Ring	100	100
Planet	40(3)	36(4)
Sun	20	28

under time-varying speed conditions and all the gears are healthy. The sampling frequency is set as 20 kHz and the signal collection lasts for 30 s. The collected waveform is shown in Figure 19 (a). The f_{ISRF} changes from 40 Hz to 60 Hz and then reverts to 40 Hz, as shown in Figure 19 (b). The meshing frequency of the planetary gearbox stage 1 is calculated as $f_{\mathrm{mesh1}} = 100/27 f_{\mathrm{ISRF}}$. Once an unexpected failure occurs, sidebands of the meshing frequency will be created.

Then, the proposed method is applied to process the vibration signal. The result for searching for the angle using the proposed chirp-rate matching strategy is plotted in Figure 19 (c), where the red line represents the estimated angles and the blue one denotes the true angles calculated by directly using the collected f_{ISRF}. It can be seen that the estimated angles are consistent with the true angles, demonstrating the effectiveness of the proposed matching strategy.

Similarly, the signal is also processed using STFT, MLCT, STFT-based SET, and MLCSET. The analysis results of different TFA methods are given in Figure 20 (a)–(d). The local zooms are also plotted to reveal details of the TFR. It can be seen from the local zooms that the proposed method could generate a TFR with the sharpest IF ridges and highest energy concentration levels. Then, IF extraction is performed, as illustrated in Figure 21, where the instantaneous shaft rotation frequency f_{ISRF}, its harmonics, and the gear meshing frequency f_{mesh1} are successfully extracted from the

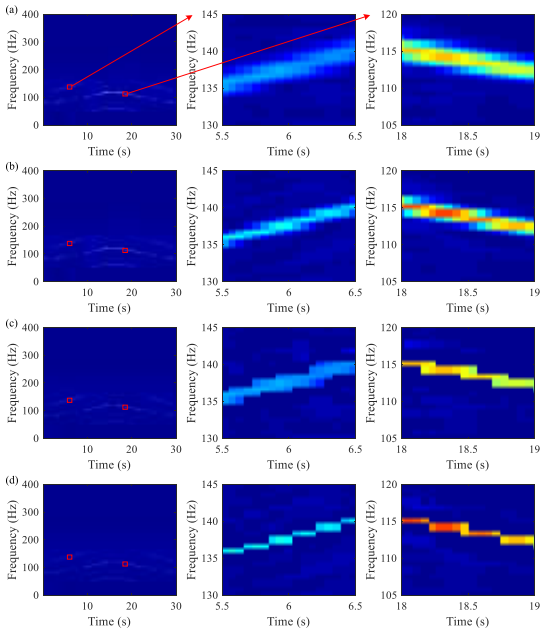

FIGURE 20. Analyzing results of planetary gearbox signal and local zooms on the right: (a) analyzing results using STFT, (b) analyzing results using MLCT, (c) analyzing results using STFT-based SET, (d) analyzing results using MLCSET.

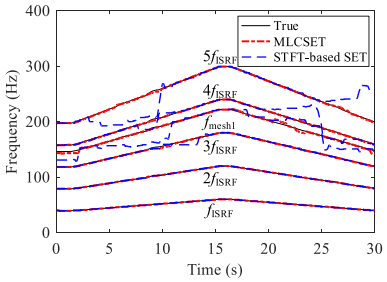

FIGURE 21. The instantaneous frequency estimation results using different methods (black: true; red: proposed MLCSET; blue: SET).

TFR obtained using the proposed MLCSET. However, the IF ridges detected from the TFR of the original SET deviate from the actual ones for the meshing frequency, and the fourth and fifth instantaneous shaft rotation frequencies.

The MREs of the detected IF ridges are also calculated to quantitatively evaluate the performance of the different methods, as shown in Table 5. According to Table 5, distinct differences in the extraction of the instantaneous shaft rotation frequency and its second harmonic do not exist between the proposed MLCSET and STFT-based SET. However, the proposed method outperforms the original SET for the extraction of the meshing frequency, and the fourth and fifth instantaneous shaft rotation frequency. The MREs of the meshing frequency, and the fourth and fifth instantaneous shaft rotation frequency extracted from the TFR of MLCSET, are much lower than those of the STFT-based SET. By observing Figure 20 (d) and Figure 21, no sidebands of meshing frequency can be identified, indicating that the planetary gearbox is in healthy condition.

TABLE 5. The mean relative errors of detected IF ridges to true IFs.

MREs of TFA methods \ Extracted IF ridges	f_{ISRF}	$2f_{ISRF}$	$3f_{ISRF}$	f_{mesh1}	$4f_{ISRF}$	$5f_{ISRF}$
MLCSET	0.48 %	0.23 %	0.33 %	0.63 %	0.27 %	0.24 %
STFT-based SET	0.49 %	0.23 %	0.67 %	5.42 %	3.07 %	5.51 %

V. CONCLUSION

In this paper, a new TFA method called MLCSET is proposed to improve the readability of TFRs for rotating machinery fault diagnosis under time-varying speed conditions. In comparison to the traditional SET, the main advantages of the proposed method are reflected by the adaptive chirp-rate matching strategy, which improves the energy concentration level of the TFR and the integration with SET for further sharpening the IF ridges. The matching linear chirplet strategy is devised to address the TF blurriness when analyzing signals with rapidly time-varying features and then boost the readability of the original TFR. On one hand, more detailed time-varying features with weak energies from the original signal can be revealed; on the other hand, more accurate extraction operators can be obtained for SETs. By embedding the matching strategy into the SET to form the proposed MLCSET, an improved TFR—with improved energy concentration levels and sharper IF ridges—can then be generated, paving the way for the use of IF ridge extraction for rotating machinery fault diagnosis.

The major advantages of proposed method include: (a) an adaptive chirp-rate matching strategy that enhances the TF energy concentration level for multiple frequency components; (b) the proposed strategy, embedded in the SET, further boosts the TFR for sharper IF ridges and more accurate IF extraction. The simulated and experimental signals reveal the effectiveness of the proposed MLCSET method for TFR readability improvement and rotating machinery health condition monitoring.

ACKNOWLEDGMENT

The authors would like to thank Lab E026 in University of Ottawa for the data collection.

REFERENCES

[1] C. Peeters, Q. Leclère, J. Antoni, P. Lindahl, J. Donnal, S. Leeb, and J. Helsen, "Review and comparison of tacholess instantaneous speed estimation methods on experimental vibration data," *Mech. Syst. Signal Process.*, vol. 129, pp. 407–436, Aug. 2019.

[2] L. Wang, G. Cai, W. You, W. Huang, and Z. Zhu, "Transients extraction based on averaged random orthogonal matching pursuit algorithm for machinery fault diagnosis," *IEEE Trans. Instrum. Meas.*, vol. 66, no. 12, pp. 3237–3248, Dec. 2017.

[3] S. Wang, X. Chen, I. W. Selesnick, Y. Guo, C. Tong, and X. Zhang, "Matching synchrosqueezing transform: A useful tool for characterizing signals with fast varying instantaneous frequency and application to machine fault diagnosis," *Mech. Syst. Signal Process.*, vol. 100, pp. 242–288, Feb. 2018.

[4] L. Cui, Z. Jin, J. Huang, and H. Wang, "Fault severity classification and size estimation for ball bearings based on vibration mechanism," *IEEE Access*, vol. 7, pp. 56107–56116, 2019.

[5] D. Wang, K.-L. Tsui, and Y. Qin, "Optimization of segmentation fragments in empirical wavelet transform and its applications to extracting industrial bearing fault features," *Measurement*, vol. 133, pp. 328–340, Feb. 2019.

[6] S. Maurya, V. Singh, and N. K. Verma, "Condition monitoring of machines using fused features from EMD-based local energy with DNN," *IEEE Sensors J.*, vol. 20, no. 15, pp. 8316–8327, Aug. 2020.

[7] W. Guo, X. Jiang, N. Li, J. Shi, and Z. Zhu, "A coarse TF ridge-guided multi-band feature extraction method for bearing fault diagnosis under varying speed conditions," *IEEE Access*, vol. 7, pp. 18293–18310, 2019.

[8] T. Wang, M. Liang, J. Li, and W. Cheng, "Rolling element bearing fault diagnosis via fault characteristic order (FCO) analysis," *Mech. Syst. Signal Process.*, vol. 45, no. 1, pp. 139–153, Mar. 2014.

[9] H. Huang, N. Baddour, and M. Liang, "A method for tachometer-free and resampling-free bearing fault diagnostics under time-varying speed conditions," *Measurement*, vol. 134, pp. 101–117, Feb. 2019.

[10] Z. Feng, M. Liang, and F. Chu, "Recent advances in time–frequency analysis methods for machinery fault diagnosis: A review with application examples," *Mech. Syst. Signal Process.*, vol. 38, no. 1, pp. 165–205, Jul. 2013.

[11] X. Jiang and S. Li, "A dual path optimization ridge estimation method for condition monitoring of planetary gearbox under varying-speed operation," *Measurement*, vol. 94, pp. 630–644, Dec. 2016.

[12] H. Huang, N. Baddour, and M. Liang, "Algorithm for multiple time-frequency curve extraction from time-frequency representation of vibration signals for bearing fault diagnosis under time-varying speed conditions," in *Proc. 29th Conf. Mech. Vibrat. Noise*, vol. 8, Aug. 2017, Art. no. V008T012A046.

[13] S. Meignen, D.-H. Pham, and S. McLaughlin, "On demodulation, ridge detection, and synchrosqueezing for multicomponent signals," *IEEE Trans. Signal Process.*, vol. 65, no. 8, pp. 2093–2103, Apr. 2017.

[14] C. Li, V. Sanchez, G. Zurita, M. Cerrada Lozada, and D. Cabrera, "Rolling element bearing defect detection using the generalized synchrosqueezing transform guided by time–frequency ridge enhancement," *ISA Trans.*, vol. 60, pp. 274–284, Jan. 2016.

[15] J. Shi, M. Liang, D.-S. Necsulescu, and Y. Guan, "Generalized stepwise demodulation transform and synchrosqueezing for time–frequency analysis and bearing fault diagnosis," *J. Sound Vib.*, vol. 368, pp. 202–222, Apr. 2016.

[16] Z. Ma, F. Lu, S. Liu, and X. Li, "An adaptive generalized demodulation method for multimedia spectrum analysis is applied in rolling bearing fault diagnosis," *IEEE Access*, vol. 8, pp. 20687–20699, 2020.

[17] I. Daubechies, J. Lu, and H.-T. Wu, "Synchrosqueezed wavelet transforms: An empirical mode decomposition-like tool," *Appl. Comput. Harmon. Anal.*, vol. 30, no. 2, pp. 243–261, Mar. 2011.

[18] F. Auger, P. Flandrin, Y.-T. Lin, S. McLaughlin, S. Meignen, T. Oberlin, and H.-T. Wu, "Time-frequency reassignment and synchrosqueezing: An overview," *IEEE Signal Process. Mag.*, vol. 30, no. 6, pp. 32–41, Nov. 2013.

[19] G. Thakur, E. Brevdo, N. S. Fu kar, and H.-T. Wu, "The synchrosqueezing algorithm for time-varying spectral analysis: Robustness properties and new paleoclimate applications," *Signal Process.*, vol. 93, no. 5, pp. 1079–1094, May 2013.

[20] T. Oberlin, S. Meignen, and V. Perrier, "Second-order synchrosqueezing transform or invertible reassignment? Towards ideal time-frequency representations," *IEEE Trans. Signal Process.*, vol. 63, no. 5, pp. 1335–1344, Mar. 2015.

[21] X. Tu, Y. Hu, F. Li, S. Abbas, Z. Liu, and W. Bao, "Demodulated high-order synchrosqueezing transform with application to machine fault diagnosis," *IEEE Trans. Ind. Electron.*, vol. 66, no. 4, pp. 3071–3081, Apr. 2019.

[22] Y. Miao, H. Sun, and J. Qi, "Synchro-compensating chirplet transform," *IEEE Signal Process. Lett.*, vol. 25, no. 9, pp. 1413–1417, Sep. 2018.

[23] G. Yu and Y. Zhou, "General linear chirplet transform," *Mech. Syst. Signal Process.*, vols. 70–71, pp. 958–973, Mar. 2016.

[24] G. Yu, M. Yu, and C. Xu, "Synchroextracting transform," *IEEE Trans. Ind. Electron.*, vol. 64, no. 10, pp. 8042–8054, Oct. 2017.

[25] Q. Wang, J. Gao, and N. Liu, "Second-order synchrosqueezing wave packet transform and its application for characterizing seismic geological structures," *IEEE Geosci. Remote Sens. Lett.*, vol. 17, no. 5, pp. 760–764, May 2020.

[26] Z. Li, J. Gao, H. Li, Z. Zhang, N. Liu, and X. Zhu, "Synchroextracting transform: The theory analysis and comparisons with the synchrosqueezing transform," *Signal Process.*, vol. 166, pp. 1–14, Jan. 2020.

[27] X. Zhu, Z. Zhang, J. Gao, B. Li, Z. Li, X. Huang, and G. Wen, "Synchroextracting chirplet transform for accurate IF estimate and perfect signal reconstruction," *Digit. Signal Process.*, vol. 93, pp. 172–186, Oct. 2019.
[28] F. Auger and P. Flandrin, "Improving the readability of time-frequency and time-scale representations by the reassignment method," *IEEE Trans. Signal Process.*, vol. 43, no. 5, pp. 1068–1089, May 1995.

ZEHUI HUA received the B.S. degree in vehicle engineering from Soochow University in 2018, where he is currently pursuing the M.S. degree in vehicle engineering. His research interests include time-frequency analysis, fault diagnosis, and the health condition monitoring of trail vehicles.

JUANJUAN SHI received the B.S. and M.S. degrees in mechanical engineering from Northwest A&F University, Xianyang, China, in 2008 and 2011, respectively, and the Ph.D. degree in mechanical engineering from the University of Ottawa, ON, Canada, in 2015. From 2012 to 2015, she was a Teaching Assistant with the University of Ottawa. Since 2016, she has been an Associate Professor with the School of Rail Transportation, Soochow University, China. Her research interests include rotating machinery condition monitoring, vibration control, and digital signal processing.

ZHONGKUI ZHU received the B.S. degree in automobile and tractor (automobile) engineering and the M.S. degree in vehicle engineering from Hefei Polytechnic University, in 1997 and 2002, respectively, and the Ph.D. degree in instrument science and technology from the University of Science and Technology of China in 2005. He is currently a Professor with the School of Rail Transportation, Soochow University. His research interests include the fault diagnosis of mechanical equipment, vehicle system dynamics and control, and vibration measurement and signal processing.